Trapping mechanisms and delayed recombination processes in scintillating Ce-doped sol-gel silica fibers

Francesca Cova[1]*, Federico Moretti[2], Christophe Dujardin[3], Norberto Chiodini[1], and Anna Vedda[1]

[1]Department of Materials Science, University of Milano - Bicocca, via Cozzi 55, 20125 Milano, Italy

[2]Lawrence Berkeley National Laboratory, 1 Cyclotron Road, Berkeley, CA 94720, USA

[3]Université de Lyon, Université Claude Bernard Lyon 1, CNRS, Institut Lumière Matière, 69622, Villeurbanne, France

* E-mail: francesca.cova@unimib.it

Abstract

The carrier trapping and recombination mechanisms occurring in Ce-doped silica fibers, produced by sol-gel technique, are investigated by combining temperature dependent steady-state X-ray excited luminescence, wavelength- and time-resolved scintillation measurements, and wavelength-resolved thermally stimulated luminescence, focusing especially on the temperature range from 10 K to 320 K.

The scintillation decay features a decay time of the order of tens of ns, characteristic of the parity and spin allowed 5d - 4f radiative transition of Ce^{3+} ions. Besides, a slow and complex decay contribution in the μs time scale is detected. We interpret these features as the radiative recombination at Ce centers of carriers freed from a continuous distribution of trapping sites in the forbidden gap, as well as to the occurrence of an athermal tunneling recombination process between traps and Ce^{3+} ions. This interpretation is reinforced by the good agreement between independent evaluations of trap depths and lifetimes obtained by both the numerical analysis of scintillation time decays and thermally stimulated luminescence experiments.

1. Introduction

Scintillators are materials able to efficiently convert ionizing radiation into ultraviolet or visible light, thus allowing the detection of highly energetic photons and particles by conventional optical sensors. Scintillating materials are widely used in several applications[1,2], ranging from high-energy physics calorimetry and astrophysics[3,4], to medical devices[5], homeland security[6], and industrial controls[7].

Scintillation light often originates from radiative transitions at intrinsic centers or dopants used as activators: therefore, a fast and efficient transport to the luminescent centers of carriers generated upon the interaction between ionizing radiation and the scintillating material is fundamental in the scintillation process. The efficiency and speed of carrier transfer through the host matrix are affected by the presence of defects, leading to trapping levels in the forbidden energy gap, which can temporarily capture migrating charge carriers, either delaying their radiative recombination at emission centers or decreasing the scintillation efficiency[8,9]. Since trapped carriers can take part in the recombination when they are thermally released, shallow traps, showing longer lifetime but in the order of the scintillation decay time, are responsible for delayed recombination processes. On the other hand, deep traps (with a lifetime much longer with respect to the scintillation decay time) can stably store the carriers. A lower overall scintillation efficiency, due to the competition with luminescent centers in charge capture, is observed. The terms shallow and deep are not uniquely defined, because the same trap in a material can be considered either shallow or deep depending on the time scale of the optical transitions[10].

Although synthesis technologies are continuously improved, a certain amount of point defects at the atomic scale is very common even for materials synthesized in highly controlled conditions. Therefore, the study of the role of defects in the scintillation mechanism becomes essential in the science of scintillators and has seen significant progress in the recent years. The presence of trapping sites has been evidenced in inorganic crystalline scintillators, both intrinsic[11,12] and extrinsic[13–15], as well as perovskite scintillators[16]. The development of a new class of organic and hybrid systems as promising materials for a wide range of applications[17–21] led to significant advancements in the study of charge-trapping phenomena in organic polymers[22], nanocrystal quantum dots[23], and metal-organic-frameworks[24]. Furthermore, the formation of defect complexes has been discovered and ascribed to a close spatial correlation between intrinsic traps and dopant ions[25,26]. However, the relationship between the presence of defects and their effects on the scintillation process is not fully understood, preventing a targeted approach to the optimization of

the synthesis procedure. Therefore, the investigation of the trapping phenomena is a crucial aspect both for the fundamental understanding of the material properties and for its application-oriented engineering.

Silica-based glass has been the subject of intense investigations, due to the wide variety of applications of this material[27–31]: it showed excellent chemical stability, good mechanical properties, easy preparation processes, doping and shaping possibilities. Indeed, silica glass recently attracted interest because it turned out to be suitable for flexible fiber-based technologies[32–36], opening its application perspectives in the sensors[37–39], lasers[40,41] and space field[42,43] as a powerful tool for innovative designs.

In some cases, scintillators based on rare earth (RE)-doped glass matrices were demonstrated to be a valid alternative to single crystals[44–46]. At first developed for remote real-time dosimetry in radiology and radiotherapy[47–51], recently scintillating silica fibers were explored as candidates for the dual-readout calorimetry approach in high-energy physics[52–57], exploiting the simultaneous detection of scintillation and Cherenkov light as a possible way to improve the energy resolution of calorimetric detectors[58]. Quartz fibers were also considered as wavelength shifters for the collection and transport of light in high-energy physics experiments[59].

In this work, we studied scintillating Ce-doped silica fibers produced by sol-gel synthesis[60,61]. This procedure allows to strictly control the luminescent centers incorporation and dispersion inside the glass matrix[44,62,63]. The synthesis process can be performed by using high purity precursors, allowing to master the level of unwanted impurities, which is an essential achievement in the improvement of the scintillation performances of this class of amorphous materials[64]. Indeed, scintillation efficiency, linearity upon dose and signal reproducibility were optimized in the past years[47,65–68].

A peculiar feature of sol-gel silica is the incorporation of Ce ions in the silica matrix mainly in the 4+ oxidation state[69,70]. In fact, the exposure of Ce-doped silica to ionizing radiation gives rise to temporary bond breaks with the consequent change in the Ce valence state: therefore, Ce^{4+} ions are temporarily reduced to Ce^{3+}, and radiative recombination occurs with the emission of scintillation light. A similar phenomenon was also observed for garnet and silicate single crystals, particularly evident when a divalent co-dopant is added, as well as for garnet optical ceramics[71–73]. The parity and spin allowed 5d - 4f transition of Ce^{3+} ions permits to achieve fast and bright luminescence in the visible region, free from thermally induced non-radiative quenching.

The in-depth analysis of the role of point defects and of their close interplay with luminescent activators in the recombination processes governing the scintillation emission is not commonly

encountered in amorphous materials, because the inhomogeneous disorder of glass leads to broadening of electronic levels related to defects[74]. In previous studies, thermally stimulated luminescence (TSL) has been used both to estimate the characteristic parameters of trapping levels and for application-oriented purposes[75–77]. We chose Ce-doped sol-gel silica as a model material to study the correlation between TSL active traps and slow tails in time-resolved scintillation. Temperature- and dose-dependent steady-state X-ray excited luminescence is combined with time-resolved scintillation measurements and wavelength-resolved TSL in order to explore the tight connection existing between delayed recombination processes and defects acting as carrier traps, due to the competition between trapping centers and luminescent ions in carrier capture. The thermal depths and the low-temperature lifetimes of traps responsible for the delayed mechanisms are evaluated. Eventually, the correlation between a continuous distribution of trap levels in Ce-doped silica and slow tails in the scintillation time decay is revealed and discussed.

2. Methods

Ce-doped silica glass with Ce concentration of 0.05 mol% is prepared by sol-gel method using tetramethylorthosilicate (TMOS) and Ce(III) as precursors. Alcogels are formed after gelation and subsequently dried in a thermostatic chamber for a few weeks. The obtained xerogels are densified at 1225 °C in an oxidizing atmosphere (O_2), to produce Ce-doped preforms. Cylindrical fibers are then drawn at a temperature of about 2200 °C by Polymicro Technologies (Phoenix, USA), using a fluorinated SiO_2 cladding around the Ce-doped core to guarantee a good light guiding by the core-cladding interface: the core diameter is 0.60 mm and the total fiber diameter is 0.75 mm. Fibers are left uncoated and cut into 20 mm long pieces for measurement purposes.

Radio-luminescence (RL) measurements are performed as a function of temperature from 10 K to 320 K, using a custom apparatus featuring a liquid nitrogen-cooled, back-illuminated and UV-enhanced, charge-coupled device (CCD) detector (Jobin-Yvon Spectrum One 3000) coupled to a monochromator (Jobin-Yvon Triax 180) with a 100 lines/mm grating, as detection system. The excitation is obtained by unfiltered X-ray irradiation through a beryllium window, using a Philips PW2274 X-ray tube with tungsten anode operated at 20 kV.

Time-resolved emission spectra under X-ray excitation are obtained using a pulsed laser DeltaDiode-405L from Horiba emitting at 405 nm hitting the photocathode of an X-ray tube from Hamamatsu (N5084) set at 30 kV. The emitted light was collected by a monochromator from Andor (Kymera 193i) with a grating of 300 lines/mm. Detection is performed by a hybrid photomultiplier tube (HPM

100-40c) from Becker & Hickl GmbH. Time resolved analysis is obtained using a multichannel counter MCS6A from Fast ComTec (0.8 ns/channel). A custom software drives the monochromator and records the decay time for each wavelength. The reconstruction of the time gated emission spectra are performed off-line.

The time response of the X-ray excited scintillation emission measured in the μs time scale is performed using a custom-made 40 keV pulsed X-ray system consisting of an ultrafast Ti-sapphire laser (200 fs pulses at 165 kHz, Coherent Mira), a light excited X-ray tube (Hamamatsu N5084), a Hamamatsu R3809U-50 microchannel PMT and an Ortec 9308 ps time analyzer. The impulse response function of the system is 100 ps FWHM[78]. Measurements in the 10 - 350 K temperature interval were performed by using an ARS He cryocooler. The temperature was controlled with a Lakeshore 331 controller.

Phosphorescence and wavelength-resolved TSL at cryogenic temperatures are carried out by using the same detection system as for RL measurements. Cryogenic TSL measurements are performed in the 10 - 320 K interval, with heating rate of 0.1 K/s, after 10 K X-ray irradiation up to 120 Gy. The dose values for X-ray irradiations were obtained by comparison with a calibrated ^{90}Sr-^{90}Y beta radioactive source and using optically stimulated luminescence emission from quartz crystalline powder (100-200 μm grains).

Wavelength-resolved TSL measurements above room temperature (RT) are carried out using a custom-made equipment. The heater section is custom-designed and fabricated by Tecna s.r.l., and the heating rate is 1 K/s; the detection system features a liquid nitrogen-cooled, back illuminated and UV-enhanced, Jobin-Yvon Symphony CCD detector coupled to a Jobin-Yvon Micro HR monochromator, equipped with a 150 lines/mm grating. The fibers are irradiated by a Machlett OEG50 X-ray tube with tungsten anode, operated at 20 kV.

All the emission spectra are corrected for the spectral response of the detection systems.

3. Results and Discussion

The proposed experimental approach for the investigation of the role of trapping sites consists in coupling steady-state RL and time-resolved scintillation kinetics with TSL results; it is aimed at finding the characteristic parameters of traps allowing to predict their lifetime at a given temperature and, consequently, to correlate them with the observed scintillation response.

3.1 Steady state emission: radio-luminescence

RL spectra of Ce-doped silica fibers in the 10 - 320 K range are shown in Figure 1(a): the spectra feature the characteristic emission band related to the allowed 5d - 4f radiative transition of Ce^{3+} ions peaking at around 460 nm, and no significant shape modification can be observed as a function of temperature.

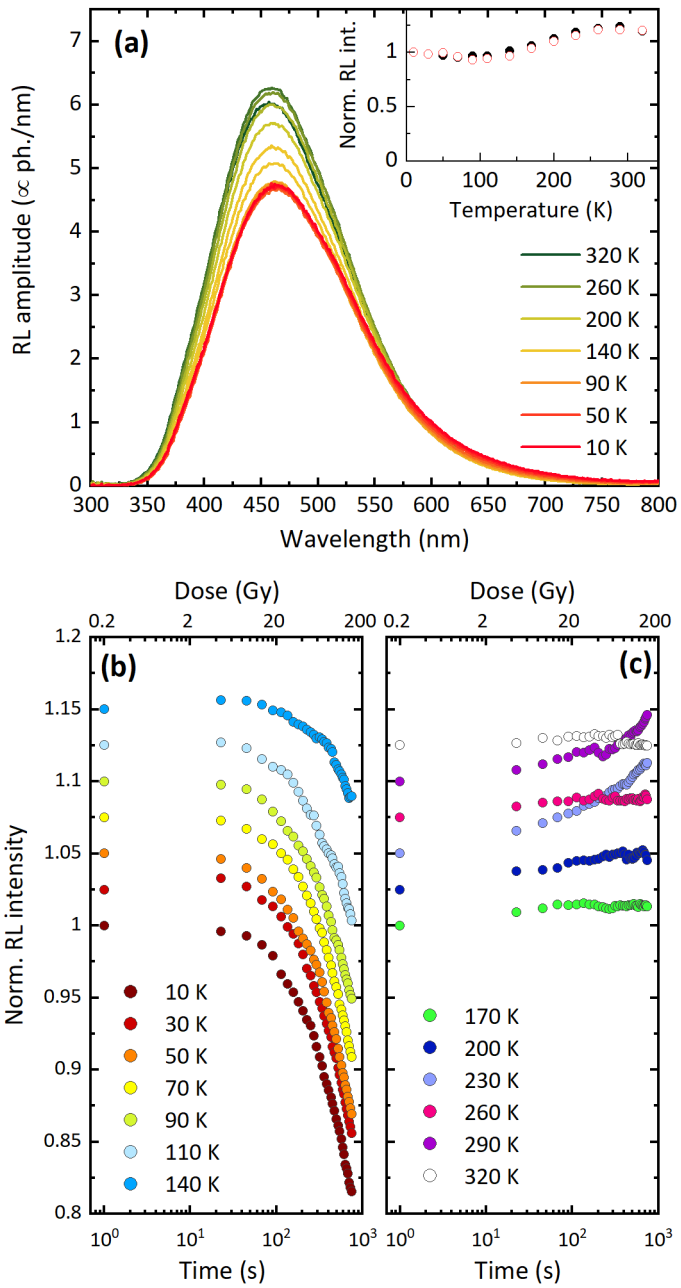

Figure 1: Top panel: RL spectra of Ce-doped silica fibers under 20 kV X-ray excitation as a function of temperature. The inset shows the temperature dependence of the RL intensity, evaluated as the integral of Ce emission in the 350 - 700 nm range. Full symbols: temperature sequence from 320 K to 10 K. Open symbols: temperature sequence from 10 K to 320 K.

Bottom panels: RL intensity as a function of time (bottom x-axis) and dose (top x-axis) during X-ray irradiation at different temperatures. In panel (b) and (c) the measurements obtained from 10 K to 140 K and from 170 K to 320 K are reported, respectively. The measurements have been performed in the following random temperature sequence: 290, 230, 170, 30, 200, 110, 70, 10, 260, 140, 90, 50, and 320 K. The curves are normalized to their initial value and shifted on the y-axis for better clarity.

In the inset, the temperature dependence of the integral of the RL emission band in the 350 - 700 nm range is reported in two different sequences, by temperature decreasing and temperature increasing, in order to remove potential thermally stimulated contribution, respectively. The non-trivial trend, observed in both sequences, can be ascribed to the presence of defects that compete with Ce recombination centers in free carrier capture, whose stability strongly depends upon temperature, as already observed for Ce-doped bulk silica[67].

Sequences of RL measurements as a function of X-ray cumulated dose are performed on Ce-doped silica fibers by varying the temperature from 10 K to 320 K. The results are displayed in Figures 1(b) and 1(c) as a function of both exposure time and dose, the dose being proportional to the irradiation time considering a constant dose rate of about 0.2 Gy/s. Data points represent the integral of the RL emission spectra in the 350 - 700 nm range, corresponding to the Ce^{3+} emission band. After each sequence, the fibers are heated up to 320 K to empty all the filled traps and restore the pristine RL response. Two temperature regimes can be clearly distinguished: in panel (b), for T < 150 K, a decrease of the RL intensity upon cumulated dose is evident, that reaches almost 20 % at the minimum temperature of 10 K. On the other hand, in panel (c), for T > 150 K, an increase of the RL intensity can be observed, mostly pronounced at 230 K: the flat behavior of the RL sequence at 260 K and 320 K might be due to the incomplete depletion of the traps filled in the preceding measurement.

In the latter case, the hysteresis phenomenon, also commonly called “bright-burn”, occurs, well-known for scintillators and already observed in garnets[13], aluminum oxides[79], as well as pyrosilicates[80], and oxyorthosilicates[72,81]. In fact, the enhancement of the RL sensitivity as a function of irradiation dose has been proven to be a common characteristic of several scintillators, whose dose dependence and overall relevance are peculiar of each material and might reflect the different concentrations, stability, and capture cross-sections of carrier traps as well as their spatial correlation with the recombination centers[13,82]. The occurrence of bright-burn is ascribed to the progressive filling of traps during irradiation, leading to an increase of the radiative recombination probability of free carriers due to a reduced competition between defects and emission centers in free carrier capture: once a dynamical equilibrium is achieved between the two trapping processes,

a saturation level is reached. Moreover, a close spatial proximity between traps and luminescent centers is expected to enhance the bright-burn effect because they directly compete in capturing the carriers during the very final stages of their path, when their energy is too low to produce additional lattice ionization and excitation.

On the other hand, there are only few evidences in the scintillation literature of a decrease of the RL sensitivity with prolonged exposure to irradiation[83], like it is observed here for Ce-doped silica at low temperature. The observed phenomenon can be explained by taking into account the formation of radiation-induced defects, even at a relatively low irradiation dose, which could lead to self-absorption of the emitted light, but are unstable above 150 K. In this situation, the effect does not affect the light production but the light collection. Indeed, the formation of radiation-induced color centers at RT has been previously observed for Ce- and Pr-doped silica fibers[64,84], after exposure to high levels of ionizing radiation. Alternatively, we could suggest that defects created by irradiation in the proximity of Ce ions might induce a charge compensation, inhibiting electron capture by Ce^{4+} and the subsequent $Ce^{4+} \rightarrow Ce^{3+*}$ modification.

3.2 Time evolution of the luminescence emission: scintillation and phosphorescence

Wavelength-resolved scintillation time decay profile of Ce-doped silica fibers is displayed in Figure 2: in the 1.6 μs time gate, only Ce^{3+} emission is detected, as better shown in the bottom inset of the Figure, and no additional emissions from impurities or intrinsic defects are observed even at times much longer than the Ce^{3+} decay time. Interestingly, by integrating the signal in different time windows from 50 ns up to 1.6 μs, a slight shift of about 15 nm of the band maximum position occurs, with a non-monotonic trend, as reported in the top inset of the Figure. Considering that the main decay time of the light promptly emitted by the 5d - 4f transition of Ce ions for our relatively low concentration range of 0.05 % is about 80 ns[44], such effect, extending at longer times, could possibly be ascribed to some variations in the Ce environment related to the close proximity of some Ce ions with defects responsible for a slow decay component, as it will be presented below.

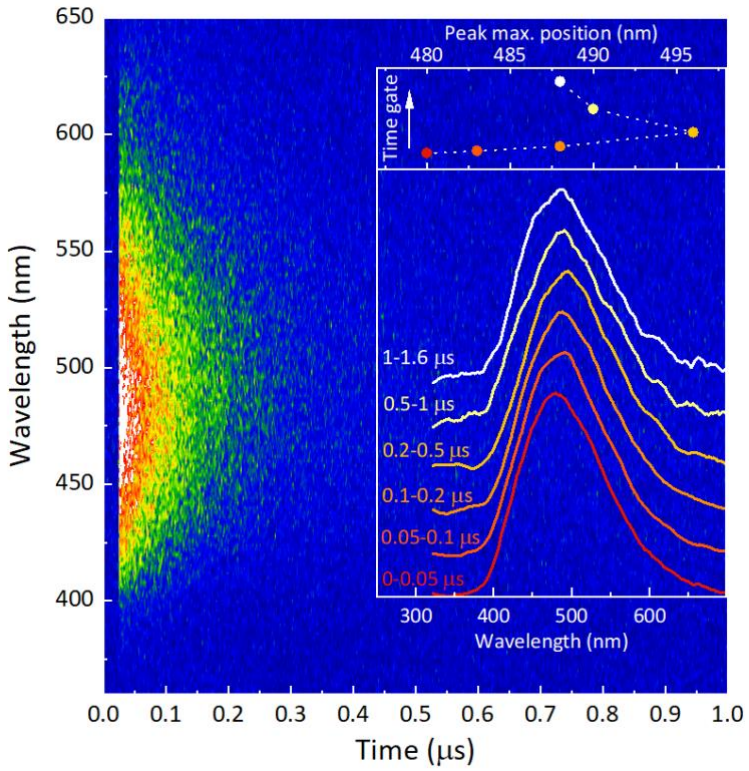

Figure 2: Wavelength-resolved scintillation time decay of Ce-doped silica fibers. In the bottom inset, the emission spectra are shown for different time gates reported in the labels. In the top inset, a non-monotonic shift of the position of the band maximum as a function of the time gate is clearly visible. The dashed line is a guide for the eye.

In order to carry out an exhaustive analysis of the scintillation decay of Ce-doped silica fibers, spectrally unresolved curves in an extended time interval of 5 µs are reported in Figure 3(a) as a function of decreasing temperature and fitted in order to identify the various components of the decay: fit to the experimental data are reported in Figure 3(b) for 30 K and 290 K, as examples. Two separated temperature regions are distinguished in the following analysis. For T < 200 K, the best function reproducing the experimental data consists in the sum of two exponential contributions and a power law decay component[85], according to Eq. 1,

$$I(t) = A_1 exp\left[-\left(\frac{t-t_0}{\tau_1}\right)\right] + A_2 exp\left[-\left(\frac{t-t_0}{\tau_2}\right)\right] + B(t-t_0)^{-p} \qquad (1)$$

where p converges to about 0.85 and t_0 is negligible in the considered time window. For T > 200 K, the experimental data are better reproduced by the sum of three exponential contributions, as described by Eq. 2:

$$I(t) = \sum_{i=1}^{3} A_i exp\left(-\frac{t}{\tau_i}\right) \qquad (2)$$

Decay time constants (τ_i) and relative weights, evaluated from the fit analyses, are reported as a function of temperature in Figures 3(c) and 3(d), respectively. In the whole temperature range, the time decay consists in a three-stage process characterized by an initial fast contribution with a decay time of about 45 ns and by a leading component of about 125 ns; the third component follows a power law function below 200 K and an exponential decay in the µs time range at higher temperatures. The fastest component can be ascribed to the decay of Ce^{3+} luminescence, accompanied by non-radiative transitions and/or energy transfer processes that introduce distortions in the initial part of the curve, with respect to the single exponential decay expected for the 5d - 4f transition of Ce^{3+} ions. On the other hand, the slower tails in the scintillation decay can be attributed to the trapping of free carriers at shallow traps, which causes a delay in the recombination at luminescent centers. In Figure 3(d), the vertical dashed line provides a distinction between the three-exponential analysis (on the right) and the results obtained by the fit procedure using Eq. 1 (on the left side). While the main contribution (w_2) does not feature any temperature dependence, an increase of the relative weight of the slow component (w_3), coupled to a decrease of the weight of the faster one (w_1) with increasing temperature, is clearly visible, thus confirming the trend previously observed in the curves of Figure 3(a).

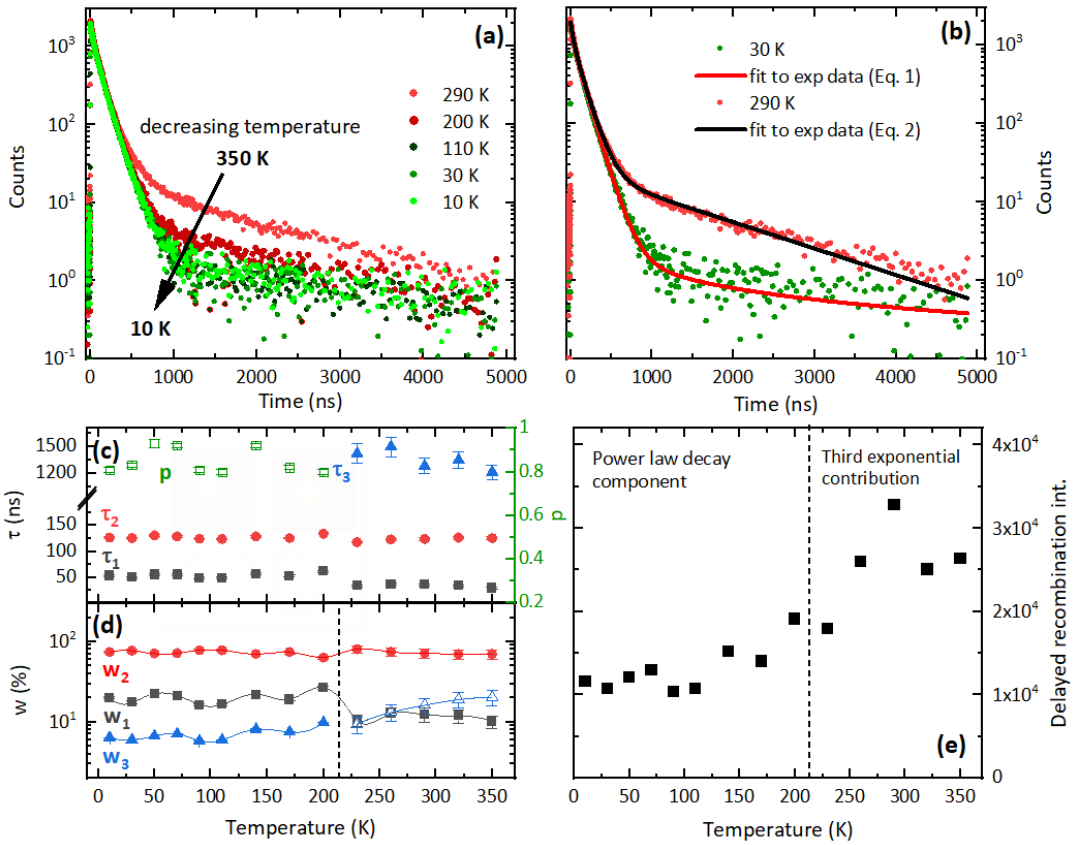

Figure 3: panel (a), spectrally unresolved scintillation decay profiles of Ce-doped silica fibers as a function of temperature, obtained by exciting with a pulsed X-ray source. Panel (b), fit to the experimental data are reported as an example for two selected temperature values, namely 290 K and 30 K: curves obtained from 200 K to 350 K are satisfactorily analyzed using the sum of three exponential components, whereas below 200 K, the sum of two exponential components and a hyperbolic decay is needed to reconstruct the data. The goodness of the fit is evaluated by means of the χ^2 test that returned reduced χ^2 values of 2.5 and 0.4 for the two models, respectively. Panel (c), temperature dependence of the time constants of the decay and of the parameter *p* of the power law function (green empty squares, right axis); panel (d), temperature dependence of the weights of the three components of the decay: error bars are within the size of data points and solid lines are guides for the eye. The delayed recombination intensity is evaluated as the integral of the third component of the decay in the 0-5 μs time range (panel e).

The delayed recombination intensity, evaluated as the integral of the third component in the entire time window considered in the measurement (5 μs), is reported in Figure 3(e) as a function of temperature: it can be considered a way to quantify the influence of traps on the recombination mechanism, thus becoming more significant as the temperature increases.

The presence of a power law decay below 200 K, and its evolution in an exponential decay in the μs time scale at higher temperatures, deserves further comments. A power law time decay can be due to either (i) a recombination process involving de-trapping to the delocalized bands of carriers from a distribution of traps, typical of disordered systems[86,87] or (ii) the occurrence of an athermal tunneling mechanism between traps and Ce luminescent centers[88–90]. Indeed, the simultaneous presence of both recombination pathways occurs in our investigated system, as discussed later.

Moreover, to extend the time scale of the picture of delayed recombination processes occurring in Ce-doped silica, isothermal phosphorescence time decays after X-ray irradiation are measured in the 10 - 320 K range and in time intervals from tens of seconds up to 1 hour; indeed, both slow tails in the scintillation decay and phosphorescence are connected to the same kind of mechanism - i.e. a delayed recombination triggered by carrier de-trapping from defects; the only difference between the two phenomena lies in the different time scales of observations.

After each measurement, the sample is heated up to 320 K to fully empty the traps filled by irradiation. The isothermal phosphorescence decays were acquired immediately after the irradiation sequence reported in Figure 1(b, c) at each given temperature; therefore, the same random temperature sequence reported in the caption of Figure 1 has been followed. Within the explored temperature range, the decays are of closely similar shape, as reported in Figure 4(a), and follow a power function of the form:

$$I(t) = A(t - t_0)^{-p} \quad (3)$$

where *I(t)* is the phosphorescence amplitude, *A* is a constant, t_0 is about 10^2 s, and $0.8 < p < 1$. The parameter *p* converges to a value close to 1 and shows a slight temperature dependence up to 260 K, as displayed in Figure 4(b). For T = 320 K, an exponential contribution is added to the power law decay, pointing towards the occurrence of de-trapping from an isolated electronic trapping level: in this case, the data for *p* and t_0 are highlighted in red in Figure 4(b).

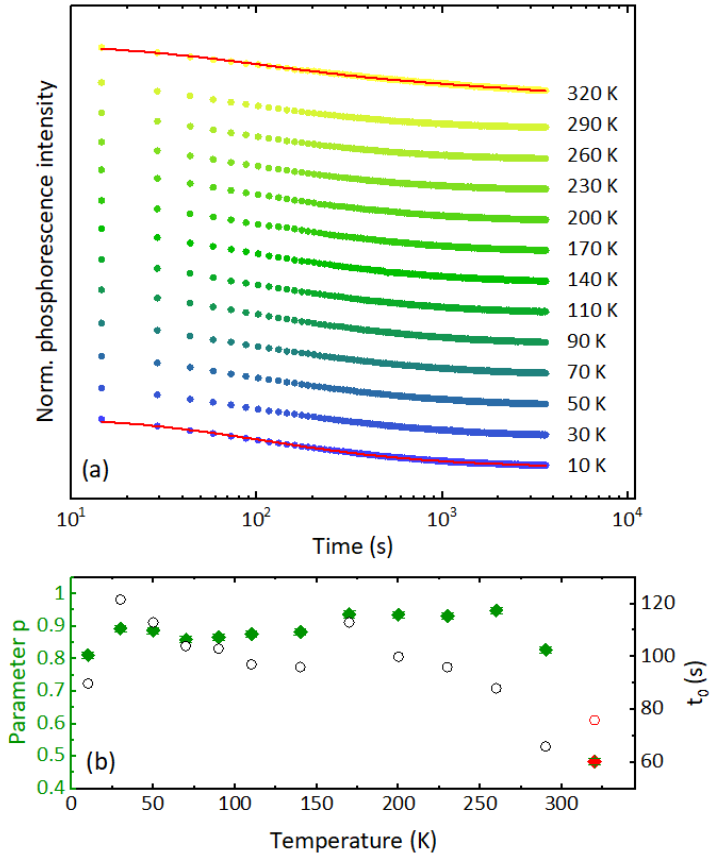

Figure 4: Panel (a): isothermal phosphorescence decays of Ce-doped silica fibers, at the temperatures marked in the figure, after X-ray irradiation. Curves are shifted on the ordinate scale for better clarity. An example of the fit is displayed for T = 10 K and T = 320 K by solid line. From 10 to 290 K, the fit function is a power law decay; for T = 320 K, an exponential contribution is added. Panel (b): temperature dependence of the parameters *p* (left y-axis, green symbols) and t_0 (right y-axis, black open symbols) of the phosphorescence decay fit, following Eq. 3. Red symbols refer to values obtained by adding an exponential contribution at 320 K. Error bars are within the size of data points.

Similarly to what discussed above for the scintillation measurements, also in the longer time scale of phosphorescence the observation of a power law decay is in principle compatible with both the existence of a trap levels distribution and the occurrence of athermal tunneling. As already pointed out before, both processes can occur together. The question concerning the type of recombination mechanism can be disentangled by considering TSL measurements described in the following.

3.3 Thermally Stimulated Luminescence

Wavelength-resolved TSL of Ce-doped silica fibers in the 10 - 700 K range is displayed in Figure 5: in panels (a) and (b), the TSL intensity is reported as a function of both emission wavelength (x-axis) and temperature (y-axis). Throughout the temperature range of the measurements, the emission is that related to the radiative 5d - 4f transition of Ce^{3+} ions, which means that carriers thermally released from traps recombine at Ce centers, and thus the TSL process in silica fibers involves defects trapping electrons.

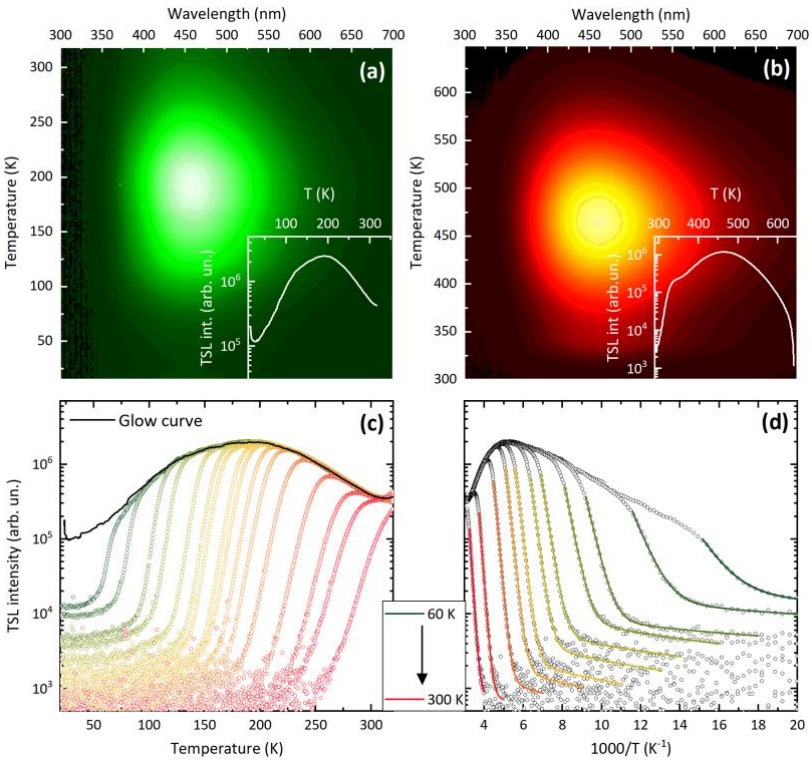

Figure 5: Top panels: wavelength-resolved TSL measurements of Ce-doped silica fibers obtained after X-ray irradiation at 10 K (panel (a)) and at RT (panel (b)). Insets: TSL glow curves obtained after integration from 350 nm to 700 nm of wavelength-resolved measurements shown in the corresponding panels.

Bottom panels: TSL glow curves after 10 K X-ray irradiation and partial cleaning at increasing T_{stop} from 60 K to 300 K (panel (c)). Arrhenius plot of the TSL measurements; continuous lines are the fits with a sum of a single exponential and a power law contribution (panel (d)).

The integration of the TSL signal over the whole emission range allows the investigation of the temperature dependence of the TSL emission; in the insets of Figure 5(a) and 5(b), TSL glow curves below and above RT are reported, respectively. A broad TSL structure is detected on the entire temperature range: the main peaks at around 190 K and 440 K, and the shoulder at 330 K are in good agreement with TSL glow curves previously measured for silica-based glasses[75,91]. In order to further elucidate the nature of the traps responsible for the TSL signal, a partial cleaning (PC)

analysis[10] is carried out in the 60 - 300 K range. We focus on this temperature region since it should reasonably include traps responsible for the slow scintillation decay contribution and the phosphorescence signal previously observed. At first, silica fibers are X-ray irradiated at 10 K with a dose of approximately 120 Gy and then pre-heated at an intermediate temperature T_{stop}. After quickly cooling down to 10 K, a TSL measurement is acquired. In Figure 5(c), the effect of the pre-heating at increasing T_{stop} on the TSL glow curve is shown. As T_{stop} increases, the TSL signal is reduced, due to the partial emptying of the traps; moreover, the TSL glow curve maximum moves towards higher temperatures, suggesting the existence of a continuous distribution of the parameters describing the trap levels. The observed narrowing of the TSL glow curve, and therefore of the population of the traps distribution, is in accordance with the fact that, at the highest temperatures considered in the current study, the slow component of the scintillation emission decay does not follow a power law function, but an exponential decay is instead observed.

The initial rise method[10] is used on all measurements after PC in order to evaluate the trap depths. When the initial rising portion of the TSL glow curve is displayed against T^{-1}, an exponential behavior is expected, due to the Arrhenius-like dependence of the TSL signal versus temperature at the beginning of the trap emptying. The thermal energy of trap levels can thus be calculated by the following expression:

$$I(T) = I_0 exp\left(-\frac{E_T}{k_B T}\right) \qquad (4)$$

where $I(T)$ is the TSL intensity, E_T the thermal energy, and k_b the Boltzmann constant. Eq. 4 is an approximation of the more complex relation between TSL intensity, temperature, and trap parameters, that is valid in the initial portion of the glow peak (up to ~ 10 % of the maximum intensity). In Figure 5(d), the Arrhenius plots of the glow curves are shown: the temperature range over which an exponential dependence over T is noticed is wider than expected and the slope of the curves increases by T_{stop} increasing. These features are consistent with a continuous distribution of trap parameters. In addition, a second term of the type BT^{-p} has been added to Eq. 4 to take into account the almost flat component particularly evident at the lowest temperatures. If we consider that a linear heating rate is employed for the TSL measurement, indeed this second term describes an athermal decay proportional to the inverse of time.

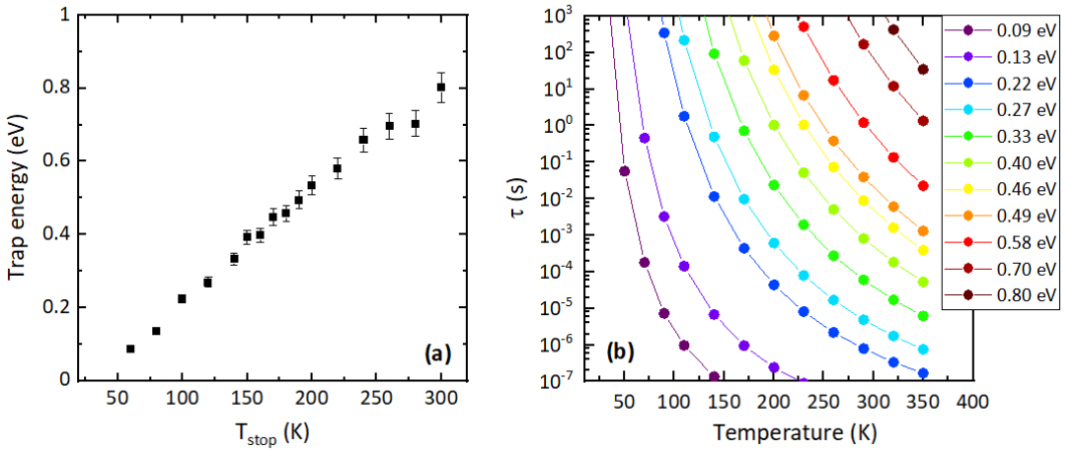

Figure 6: Panel a: distribution of trap energy values calculated by the initial rise method versus T_{stop}. Panel b: distribution of traps lifetimes at temperatures corresponding to those of scintillation decay measurements. Only values in the 10^{-7} - 10^{3} s interval are reported because only the traps with lifetime in this time scale can be reasonably related to the slow component of the scintillation decay and to the detected phosphorescence signal.

The trap energy values as a function of T_{stop} are reported in Figure 6(a) and range from approximately 0.1 eV to 0.8 eV, with an uncertainty of 5 %, according to the analysis carried out in previous works[75]. A strong peak superposition and comparable amplitudes prevent a clear appearance of distinct energy values in the curve of Figure 6(a), which simply displays a continuous distribution of energies without any modulation. The presence of a quite large trap energy distribution indicates that such electron traps can influence in a complex way the scintillation properties of the material. A wide distribution of frequency factors can also be expected, but the complex shape of the glow curve prevents a precise determination of this parameter: therefore, we chose to consider a mean frequency factor of $s = 10^{10}$ Hz[87] for the calculation of the trap lifetimes.

TSL measurements presented in Figure 5(a,b) reveal that the only recombination centers active in the TSL process are Ce ions: no emissions due to point defects of the silica matrix are visible. We remark that a similar structure in the TSL of pure bulk silica was previously observed[87], evidencing the intrinsic character of defects acting as traps.

The hole nature of recombination centers indicates that electron traps are involved in the TSL process in silica, which are indeed the dominant defects in most of Ce-doped oxide scintillators[92,93]: therefore, oxygen deficient centers seem the most probable candidates to act as electron traps in this material, as already discussed and demonstrated in the case of pure and RE-doped bulk silica[75,87,91].

We recall that our aim is to search for a possible correlation between traps observed in TSL and those responsible for scintillation slow decay components and phosphorescence signals. To this

scope, trap lifetimes are calculated at the temperatures at which scintillation and phosphorescence decays are measured, using Eq. 5:

$$\tau = s^{-1} \exp\left(\frac{E_T}{k_b T}\right) \qquad (5)$$

An extremely wide range of lifetimes is obtained; thus, in Figure 6(b) only the lifetimes of the portion of the trap distribution that lie from approximately 10^{-7} s to 10^{3} s are reported, which can reasonably be related to slow scintillation tails and phosphorescence. From Figure 6(b), it is evident that the whole trap distribution is involved in the delayed recombination processes: however, shallow traps affect more the low temperature decays, whereas the deeper traps act at higher temperatures. Moreover, we can suppose that the portion of trap distribution unstable at RT might have no role in the bright-burn phenomenon, described in the previous sections, because the equilibrium condition between trap filling and thermal release is soon reached: therefore, the deep trap population can be considered responsible for the observed unstable RL response under irradiation. TSL data display also the occurrence of an athermal tunneling recombination evident at the lowest temperatures (Figure 5(d)). Therefore, we can conclude that both a distribution of defect energy levels and an athermal tunneling mechanism can account for the detected scintillation decay.

Conclusions

This study, involving steady-state RL, time-resolved scintillation measurements, phosphorescence, and TSL, revealed the presence of a continuous distribution of trap levels in Ce-doped silica fibers; the observed electron traps are characterized by thermal energies similar to those already observed in other silica forms, ranging from around 0.1 eV up to 0.8 eV.

A close correlation between the delayed components of the scintillation decay and the existence of trapping sites is revealed; the connection between trapping centers, TSL glow curves, and delayed recombination processes reveals the complicated dynamics of carrier trapping, de-trapping, and recombination as a function of temperature.

Although the correlation between traps, scintillation, and its dynamics remains qualitative, TSL results provide a justification for the power law decay governing slow scintillation tails and isothermal phosphorescence signals. They are most probably due to the temperature dependent recombination of carriers from a portion of the detected wide trap distribution as well as to the occurrence of athermal tunneling between traps and luminescent centers. Approximate qualitative agreement between the TSL results and the analysis of the kinetics of the scintillation process is thus

demonstrated. Finally, we underline that the results presented in this work clearly show for the first time the evidence of tunneling recombination phenomena in RE-doped silica fibers.

Acknowledgements

This work was supported by the Horizon 2020 RISE Intelum project (Grant No. 644260), the EIT SPARK project (Grant No. 16290), and the ATTRACT project SCINTIGLASS (Grant No. 777222).

References

1. Dujardin, C. *et al.* Needs, Trends, and Advances in Inorganic Scintillators. *IEEE Trans. Nucl. Sci.* **65**, 1977–1997 (2018).
2. McGregor, D. S. Materials for Gamma-Ray Spectrometers: Inorganic Scintillators. *Annu. Rev. Mater. Res.* **48**, 245–277 (2018).
3. Lecoq, P. New crystal technologies for novel calorimeter concepts. *J. Phys. Conf. Ser.* **160**, 12016 (2009).
4. Di Stefano, P. C. F. Review of Direct Searches for Dark Matter and the Role of Inorganic Scintillators. *IEEE Trans. Nucl. Sci.* **63**, 528–533 (2016).
5. Ito, M., Hong, S. J. & Lee, J. S. Positron emission tomography (PET) detectors with depth-of-interaction (DOI) capability. *Biomed. Eng. Lett.* **1**, 70–81 (2011).
6. Glodo, J. *et al.* New Developments in Scintillators for Security Applications. *Phys. Procedia* **90**, 285–290 (2017).
7. Arodzero, A. *et al.* High speed, low dose, intelligent X-ray cargo inspection. *2015 IEEE Nucl. Sci. Symp. Med. Imaging Conf. NSS/MIC 2015* (2016) doi:10.1109/NSSMIC.2015.7581836.
8. *Springer Handbook of Crystal Growth*. (Springer Berlin Heidelberg, 2010). doi:10.1007/978-3-540-74761-1.
9. Korzhik, M., Tamulaitis, G. & Vasil'ev, A. N. Shallow Traps in Scintillation Materials. in 113–130 (2020). doi:10.1007/978-3-030-21966-6_4.
10. McKeever, S. W. S. *Thermoluminescence of Solids*. (Cambridge University Press, 1985). doi:10.1017/cbo9780511564994.
11. Martini, M. *et al.* Shallow traps in $PbWO_4$ studied by wavelength-resolved thermally stimulated luminescence. *Phys. Rev. B - Condens. Matter Mater. Phys.* **60**, 4653–4658 (1999).
12. Laguta, V. V. *et al.* Electron spin resonance study of self-trapped holes in $CdWO_4$ scintillator crystals. *J. Appl. Phys.* **104**, (2008).
13. Moretti, F., Patton, G., Belsky, A., Petrosyan, A. G. & Dujardin, C. Deep traps can reduce memory effects of shallower ones in scintillators. *Phys. Chem. Chem. Phys.* **18**, 1178–1184 (2016).
14. Babin, V. *et al.* Effect of Mg^{2+} ions co-doping on luminescence and defects formation processes in $Gd_3(Ga,Al)_5O_{12}$:Ce single crystals. *Opt. Mater. (Amst).* **66**, 48–58 (2017).
15. Kitaura, M. *et al.* Shallow electron traps formed by Gd^{2+} ions adjacent to oxygen vacancies in cerium-doped $Gd_3Al_2Ga_3O_{12}$ crystals. *Appl. Phys. Lett.* **113**, 41906 (2018).
16. Liu, X.-Y., Pilania, G., Talapatra, A. A., Stanek, C. R. & Uberuaga, B. P. Band-Edge Engineering To Eliminate Radiation-Induced Defect States in Perovskite Scintillators. *ACS Appl. Mater. Interfaces* (2020) doi:10.1021/acsami.0c13236.
17. Chen, Q. *et al.* All-inorganic perovskite nanocrystal scintillators. *Nature* **561**, 88–93 (2018).
18. Beaulieu, L. & Beddar, S. Review of plastic and liquid scintillation dosimetry for photon, electron, and proton therapy. *Phys. Med. Biol.* **61**, R305–R343 (2016).
19. Hajagos, T. J., Liu, C., Cherepy, N. J. & Pei, Q. High-Z Sensitized Plastic Scintillators: A Review. *Adv. Mater.* **30**, 1706956 (2018).
20. Büchele, P. *et al.* X-ray imaging with scintillator-sensitized hybrid organic photodetectors. *Nat. Photonics* **9**, 843–848 (2015).
21. Gupta, S. K. & Mao, Y. Recent advances, challenges, and opportunities of inorganic nanoscintillators. *Front. Optoelectron.* **13**, 156–187 (2020).
22. Galunov, N. *et al.* Delayed radioluminescence of some heterostructured organic scintillators. *J. Lumin.* **226**, 117477 (2020).

23. Mandal, S. *et al.* Extent of Shallow/Deep Trap States beyond the Conduction Band Minimum in Defect-Tolerant $CsPbBr_3$ Perovskite Quantum Dot: Control over the Degree of Charge Carrier Recombination. *J. Phys. Chem. Lett.* **11**, 1702–1707 (2020).
24. Fang, Z., Bueken, B., De Vos, D. E. & Fischer, R. A. Defect-Engineered Metal-Organic Frameworks. *Angew. Chemie - Int. Ed.* **54**, 7234–7254 (2015).
25. Vedda, A. *et al.* Trap-center recombination processes by rare earth activators in $YAlO_3$ single crystal host. *Phys. Rev. B* **80**, (2009).
26. Yang, B., Townsend, P. D. & Rowlands, A. P. Low-temperature thermoluminescence spectra of rare-earth-doped lanthanum fluoride. *Phys. Rev. B* **57**, 178–188 (1998).
27. Bansal, N. P. & Doremus, R. H. *Handbook of Glass Properties*. (Elsevier, 1986). doi:10.1016/C2009-0-21785-5.
28. Fanderlik, I. Silica Glass and its Applications. in *Glass Science and Technology* 2–304 (1991). doi:10.1016/B978-0-444-98755-6.50001-X.
29. Skuja, L. Optically active oxygen-deficiency-related centers in amorphous silicon dioxide. *J. Non. Cryst. Solids* **239**, 16–48 (1998).
30. Ikushima, A. J., Fujiwara, T. & Saito, K. Silica glass: A material for photonics. *J. Appl. Phys.* **88**, 1201–1213 (2000).
31. Pacchioni, G., Skuja, L. & Griscom, D. L. *Defects in SiO_2 and Related Dielectrics: Science and Technology*. (Springer Netherlands, 2000). doi:10.1007/978-94-010-0944-7.
32. Wallenberger, F. T., Watson, J. C. & Li, H. Glass Fibers. in *Composites* 27–34 (ASM International, 2001). doi:10.31399/asm.hb.v21.a0003353.
33. Brambilla, G. & Pruneri, V. Enhanced photosensitivity in silicate optical fibers by thermal treatment. *Appl. Phys. Lett.* **90**, 1–4 (2007).
34. Ballato, J., Ebendorff-Heidepriem, H., Zhao, J., Petit, L. & Troles, J. Glass and Process Development for the Next Generation of Optical Fibers: A Review. *Fibers* **5**, 11 (2017).
35. Wang, T. yun *et al.* Recent developments in novel silica-based optical fibers. *Front. Inf. Technol. Electron. Eng.* **20**, 481–489 (2019).
36. Girard, S. *et al.* Overview of radiation induced point defects in silica-based optical fibers. *Rev. Phys.* **4**, 100032 (2019).
37. Alessi, A. *et al.* Gamma and X-ray irradiation effects on different Ge and Ge/F doped optical fibers. *J. Appl. Phys.* **118**, (2015).
38. Talataisong, W., Ismaeel, R. & Brambilla, G. A Review of Microfiber-Based Temperature Sensors. *Sensors* **18**, 461 (2018).
39. Wang, P., Zhao, H., Wang, X., Farrell, G. & Brambilla, G. A Review of Multimode Interference in Tapered Optical Fibers and Related Applications. *Sensors* **18**, 858 (2018).
40. Sun, Q., Lee, T., Beresna, M. & Brambilla, G. Control of Laser Induced Cumulative Stress for Efficient Processing of Fused Silica. *Sci. Rep.* **10**, 3819 (2020).
41. Wang, S. *et al.* 2.9 μm lasing from a Ho^{3+}/Pr^{3+} co-doped AlF_3 -based glass fiber pumped by a 1150 nm laser. *Opt. Lett.* **45**, 1216 (2020).
42. Girard, S. *et al.* Recent advances in radiation-hardened fiber-based technologies for space applications. *J. Opt. (United Kingdom)* **20**, (2018).
43. Christl, M. *et al.* A solar energetic particle spectrometer (SEPS) concept. *31st Int. Cosm. Ray Conf. ICRC 2009* 1–4 (2009).
44. Vedda, A. *et al.* Insights into Microstructural Features Governing Ce^{3+} Luminescence Efficiency in Sol-Gel Silica Glasses. *Chem. Mater.* **18**, 6178–6185 (2006).
45. Sun, Y., Koshimizu, M., Kishimoto, S. & Asai, K. Synthesis and characterization of Pr^{3+}-doped glass scintillators prepared by the sol-gel method. *J. Sol-Gel Sci. Technol.* **62**, 313–318 (2012).

46. Leonard, R. L. & Johnson, J. A. Scintillator Glasses. in 1555–1584 (2019). doi:10.1007/978-3-319-93728-1_46.
47. Vedda, A. *et al.* Ce^{3+}-doped fibers for remote radiation dosimetry. *Appl. Phys. Lett.* **85**, 6356–6358 (2004).
48. Veronese, I. *et al.* Infrared luminescence for real time ionizing radiation detection. *Appl. Phys. Lett.* **105**, 61103 (2014).
49. Capoen, B. *et al.* Sol-gel derived copper-doped silica glass as a sensitive material for X-ray beam dosimetry. *Opt. Mater.* **51**, 104–109 (2016).
50. Hoehr, C. *et al.* Novel Gd^{3+}-doped silica-based optical fiber material for dosimetry in proton therapy. *Sci. Rep.* **9**, 4–11 (2019).
51. Bahout, J. *et al.* Cu/Ce-Co-Doped silica glass as radioluminescent material for ionizing radiation dosimetry. *Materials (Basel).* **13**, (2020).
52. Pauwels, K., Lucchini, M., Benaglia, A. & Auffray, E. Calorimeter Designs Based on Fibre-Shaped Scintillators. in *Springer Proceedings in Physics* 231–241 (Springer International Publishing, 2017). doi:10.1007/978-3-319-68465-9_14.
53. Akchurin, N. & Wigmans, R. Quartz fibers as active elements in detectors for particle physics. *Rev. Sci. Instrum.* **74**, 2955–2972 (2003).
54. Akchurin, N. *et al.* Cerium-doped fused-silica fibers as wavelength shifters. *J. Instrum.* **14**, (2019).
55. Akchurin, N. *et al.* Cerium-doped fused-silica fibers for particle physics detectors. *J. Instrum.* **15**, (2020).
56. Akchurin, N. *et al.* Cerium-doped scintillating fused-silica fibers. *J. Instrum.* **13**, P04010–P04010 (2018).
57. Akchurin, N. *et al.* Radiation-hardness studies with cerium-doped fused-silica fibers. *J. Instrum.* **14**, P03020–P03020 (2019).
58. Cova, F. *et al.* Dual Cherenkov and Scintillation Response to High-Energy Electrons of Rare-Earth-Doped Silica Fibers. *Phys. Rev. Appl.* **11**, 024036 (2019).
59. Becker, R. *et al.* Proof-of-principle of a new geometry for sampling calorimetry using inorganic scintillator plates. *J. Phys. Conf. Ser.* **587**, 012039 (2015).
60. Brinker, C. J. & Scherer, G. W. *Sol-Gel Science*. (Elsevier, 1990). doi:10.1016/C2009-0-22386-5.
61. Ciriminna, R. *et al.* The Sol–Gel Route to Advanced Silica-Based Materials and Recent Applications. *Chem. Rev.* **113**, 6592–6620 (2013).
62. Reisfeld, R., Patra, A., Panczer, G. & Gaft, M. Spectroscopic properties of cerium in sol–gel glasses. *Opt. Mater. (Amst).* **13**, 81–88 (1999).
63. Di Martino, D. *et al.* Evidences of Rare Earth Ion Aggregates in a Sol-Gel Silica Matrix:~ The Case of {C}erium and {G}adolinium. *Chem. Mater.* **16**, 3352–3356 (2004).
64. Cova, F. *et al.* Radiation hardness of Ce-doped sol-gel silica fibers for high energy physics applications. *Opt. Lett.* **43**, 903 (2018).
65. Chewpraditkul, W. *et al.* Luminescence and scintillation of Ce^{3+}-doped high silica glass. *Opt. Mater. (Amst).* **34**, 1762–1766 (2012).
66. Chiodini, N. *et al.* High-efficiency SiO_2:Ce3+ glass scintillators. *Appl. Phys. Lett.* **81**, 4374–4376 (2002).
67. Vedda, A. *et al.* Luminescence properties of rare-earth ions in SiO_2 glasses prepared by the sol-gel method. *J. Non-Cryst. Solids* **345**–**346**, 338–342 (2004).
68. Al Helou, N. *et al.* Radioluminescence and optically stimulated luminescence responses of a cerium-doped sol-gel silica glass under X-Ray Beam Irradiation. *IEEE Trans. Nucl. Sci.* **65**, 1591–1597 (2018).

69. Fasoli, M. *et al.* Effect of reducing sintering atmosphere on Ce-doped sol-gel silica glasses. *J. Non. Cryst. Solids* (2009) doi:10.1016/j.jnoncrysol.2009.01.043.
70. Moretti, F. *et al.* Incorporation of Ce^{3+} in crystalline Gd-silicate nanoclusters formed in silica. *J. Lumin.* (2012) doi:10.1016/j.jlumin.2011.09.016.
71. Dantelle, G. *et al.* Research on Efficient Fast Scintillators: Evidence and X-Ray Absorption Near Edge Spectroscopy Characterization of Ce^{4+} in Ce^{3+}, Mg^{2+}-Co-Doped $Gd_3Al_2Ga_3O_{12}$ Garnet Crystal. *Phys. Status Solidi Basic Res.* **257**, 1–7 (2020).
72. Blahuta, S., Bessière, A., Gourier, D., Ouspenski, V. & Viana, B. Effect of the X-ray dose on the luminescence properties of Ce:LYSO and co-doped Ca,Ce:LYSO single crystals for scintillation applications. *Opt. Mater.* **35**, 1865–1868 (2013).
73. Liu, S. *et al.* Towards Bright and Fast $Lu_3Al_5O_{12}$:Ce,Mg Optical Ceramics Scintillators. *Adv. Opt. Mater.* **4**, 731–739 (2016).
74. Alessi, A., Kuhnhenn, J., Buscarino, G., Di Francesca, D. & Agnello, S. The relevance of point defects in studying silica-based materials from bulk to nanosystems. *Electron.* **8**, (2019).
75. Vedda, A. *et al.* Thermally stimulated luminescence of Ce and Tb doped SiO_2 sol-gel glasses. *J. Non-Cryst. Solids* **351**, 3699–3703 (2005).
76. Yusoff, A. L., Hugtenburg, R. P. & Bradley, D. A. Review of development of a silica-based thermoluminescence dosimeter. *Radiat. Phys. Chem.* **74**, 459–481 (2005).
77. Bradley, D. A. *et al.* Review of doped silica glass optical fibre: Their TL properties and potential applications in radiation therapy dosimetry. *Appl. Radiat. Isot.* **71**, 2–11 (2012).
78. Derenzo, S. *et al.* New scintillators discovered by high-throughput screening. *Nucl. Instrum. Methods Phys. Res., Sect. A* **652**, 247–250 (2011).
79. Rodriguez, M. G., Denis, G., Akselrod, M. S., Underwood, T. H. & Yukihara, E. G. Thermoluminescence, optically stimulated luminescence and radioluminescence properties of Al_2O_3:C,Mg. *Radiat. Meas.* **46**, 1469–1473 (2011).
80. Dell'Orto, E., Fasoli, M., Ren, G. & Vedda, A. Defect-Driven Radioluminescence Sensitization in Scintillators: The Case of $Lu_2Si_2O_7$:Pr. *J. Phys. Chem. C* **117**, 20201–20208 (2013).
81. Cecilia, A. *et al.* Studies of LSO:Tb radio-luminescence properties using white beam hard X-ray synchrotron irradiation. *Radiat. Eff. Defects Solids* **164**, 517–522 (2009).
82. Moretti, F. *et al.* Radioluminescence Sensitization in Scintillators and Phosphors: Trap Engineering and Modeling. *J. Phys. Chem. C* **118**, 9670–9676 (2014).
83. Blahuta, S., Viana, B., Bessière, A., Mattmann, E. & LaCourse, B. Luminescence quenching processes in Gd_2O_2S:Pr^{3+},Ce^{3+} scintillating ceramics. *Opt. Mater.* **33**, 1514–1518 (2011).
84. Cova, F. *et al.* Optical properties and radiation hardness of Pr-doped sol-gel silica: Influence of fiber drawing process. *J. Lumin.* (2017) doi:10.1016/j.jlumin.2017.07.045.
85. Huntley, D. J. An explanation of the power-law decay of luminescence. *J. Phys. Condens. Matter* **18**, 1359–1365 (2006).
86. Randall, J. T. & Wilkins, M. H. Phosphorescence and electron traps II. The interpretation of long-period phosphorescence. *Proc. R. Soc. London. Ser. A. Math. Phys. Sci.* **184**, 390–407 (1945).
87. Martini, M. *et al.* Radiation induced trap levels in SIMOX oxides: low temperature thermally stimulated luminescence. *{IEEE} Trans. Nucl. Sci.* **45**, 1396–1401 (1998).
88. Fabeni, P. *et al.* Tunneling recombination processes in $PbWO_4$ crystals. *Phys. Status Solidi Curr. Top. Solid State Phys.* **4**, 918–921 (2007).
89. Pagonis, V., Bernier, S., Vieira, F. M. dos S. & Steele, S. The effect of crystal size on tunneling phenomena in luminescent nanodosimetric materials. *Nucl. Instruments Methods Phys. Res. Sect. B Beam Interact. with Mater. Atoms* **412**, 198–206 (2017).
90. Vedda, A. & Fasoli, M. Tunneling recombinations in scintillators, phosphors, and dosimeters.

Radiat. Meas. **118**, 86–97 (2018).
91. Veronese, I. *et al.* Phosphorescence of SiO_2 optical fibres doped with Ce^{3+} ions. *Phys. status solidi* **4**, 1024–1027 (2007).
92. Nikl, M. *et al.* Shallow traps and radiative recombination processes in $Lu_3Al_5O_{12}$:Ce single crystal scintillator. *Phys. Rev. B* **76**, (2007).
93. Blahuta, S., Bessiere, A., Viana, B., Dorenbos, P. & Ouspenski, V. Evidence and Consequences of Ce^{4+} in LYSO:Ce,Ca and LYSO:Ce,Mg Single Crystals for Medical Imaging Applications. *{IEEE} Trans. Nucl. Sci.* **60**, 3134–3141 (2013).

Table of Contents Image